JOURNAL OF GEOPHYSICAL RESEARCH, VOL. 102, NO. E4, PAGES 9051–9067, APRIL 25, 1997

# A simplified three-dimensional model for Martian climate studies

Robert M. Haberle,[1] Howard Houben,[2] Jeffrey R. Barnes,[3] and Richard E. Young[1]

**Abstract.** We describe a simplified physics approach to generating time-varying global wind and temperature fields suitable for conducting transport studies on Mars. The goal is to develop a computationally fast algorithm that will enable long-term simulations of the planet's climate system. Thus we use a three-dimensional log-pressure global spectral model forced with a simplified physics package based on Newtonian cooling and Rayleigh friction. We examine the model's performance at northern winter solstice for clear and dusty conditions and find that the simulated mean meridional circulation and transient eddies compare well with a more sophisticated general circulation model by tuning a single parameter: the thermal damping time. Best results are obtained for a thermal damping time of 2 days for clear conditions and 1 day for dusty conditions.

## Introduction

The purpose of this paper is to describe a simplified three-dimensional (3-D) primitive equation model we have been developing for application to Martian climate studies. Our immediate goal is to use the wind and temperature fields simulated by the model to study the role of transport in the current seasonal water cycle. Our approach has been to develop as fast and as simple a model as possible, but one which includes the main elements of the large-scale circulation. Speed is important because multiannual simulations are required. Simplicity is important because the water cycle is complex and is best approached with a hierarchy of increasingly sophisticated models.

For example, *Davies* [1981] constructed a one-dimensional (latitude) diffusive model of the Martian water cycle and concluded there was no net annual change in the size of residual north polar ice cap. Water sublimed and transported away from the cap during summer was returned and precipitated during winter (see *Jakosky* [1985] and *Jakosky and Haberle* [1992] for reviews of the current water cycle). However, using a similar model, *Jakosky* [1983] concluded otherwise. In his view, a net transfer of water from north to south occurs each year. The reason these conclusions are so different is due to the different assumptions regarding atmospheric transport. Davies assumed a mixing coefficient that varied with season, while Jakosky did not. Thus more sophisticated circulation models were needed, and so *Haberle and Jakosky* [1990] applied a two-dimensional (2-D) advective model (latitude and height) to the problem. However, while they were able to show that water is transported away from the north polar cap during summer, they were unable to determine if it returned during winter since 2-D models cannot simulate the effects of longitudinally asymmetric motions (eddies), and since eddies, at least traveling eddies, are known to be prominent features of the midlatitude winter circulation [*Barnes*, 1980, 1981]. Thus the time has come for a full three-dimensional simulation.

For this purpose we have adapted the spectral model of *Young and Villere* [1985] to Mars. Spectral models can run considerably faster than finite difference models since they are generally time-differenced using implicit techniques [e.g., *Haltiner and Williams*, 1980], and they can be severely truncated in the zonal direction and still be useful for climate modeling [e.g., *Held and Suarez*, 1978]. This is particularly true of the Martian atmosphere where the small planetary radius (as compared to Earth) assures that the dominant eddies are of low wavenumber, as will be seen below. Spectral models are also easier to diagnose than grid point models because the fields are represented in terms of spherical harmonics.

In adapting the model to Mars we use the simplest possible representation of heating and friction: Newtonian cooling and Rayleigh friction. At this point, our goal is not to construct a full up general circulation model (GCM) but instead is to conduct mechanistic studies to determine the relative contributions of the two main components of the general circulation: the mean meridional circulation and the transient baroclinic eddies. Thus the model can be viewed as a bridge between 2-D models and GCMs.

In this paper we describe the model and discuss its results. The results presented are for northern winter solstice, the time of year water can be returned to the north cap and global scale dust storms can occur. In judging the model, we compare it to observations, and to the NASA Ames GCM

[1]Space Science Division, NASA Ames Research Center, Moffett Field, California.

[2]Space Physics Research Institute, Sunnyvale, California.

[3]Department of Atmospheric Sciences, Oregon State University, Corvallis.



Paper number 97JE00383.
0148-0227/97/97JE-00383$09.00

of *Pollack et al.* [1990], whose mean meridional circulation and midlatitude transient eddy characteristics have been recently documented by *Haberle et al.* [1993] and *Barnes et al.* [1993], respectively. In general, we find that the climate model simulates well the intensity and structure of the mean meridional circulation and the basic features of midlatitude eddies.

## Model Description

### Dynamics

The dynamical part of the model was developed during the 1980s at Ames Research Center by R. E. Young. Since then the model has been applied to a variety of problems including baroclinic instability [*Young and Villere,* 1985; *Barnes and Young,* 1992] and aerosol transport in the Earth's stratosphere [*Young et al.,* 1994]. However, a detailed description of the basic equations and numerical techniques has yet to appear. Since we anticipate wide application of this model to Martian climate issues, we present here a more detailed description for future reference.

The model's dynamics are governed by the flux form of the primitive equations cast in a spherical log-pressure coordinate system. These equations are

$$\frac{\partial(pu)}{\partial t}+\frac{1}{a\sin\theta}\frac{\partial(\sin\theta pvu)}{\partial\theta}+\frac{1}{a\sin\theta}\frac{\partial(pu^2)}{\partial\varphi}+\frac{\partial(puw)}{\partial z}$$
$$=-pv\left(f+\frac{u\cot\theta}{a}\right)-\frac{1}{a\sin\theta}\frac{\partial(p\Phi)}{\partial\varphi}-\frac{H}{a}\frac{\partial}{\partial z}\left(\frac{\Phi}{\sin\theta}\frac{\partial p}{\partial\varphi}\right)$$
$$+\text{damping terms,} \quad (1)$$

$$\frac{\partial(pv)}{\partial t}+\frac{1}{a\sin\theta}\frac{\partial(\sin\theta pv^2)}{\partial\theta}+\frac{1}{a\sin\theta}\frac{\partial(pvu)}{\partial\varphi}+\frac{\partial(pvw)}{\partial z}$$
$$=pu\left(f+\frac{u\cot\theta}{a}\right)-\frac{1}{a}\frac{\partial(p\Phi)}{\partial\theta}-\frac{H}{a}\frac{\partial}{\partial z}\left(\Phi\frac{\partial p}{\partial\theta}\right)$$
$$+\text{damping terms,} \quad (2)$$

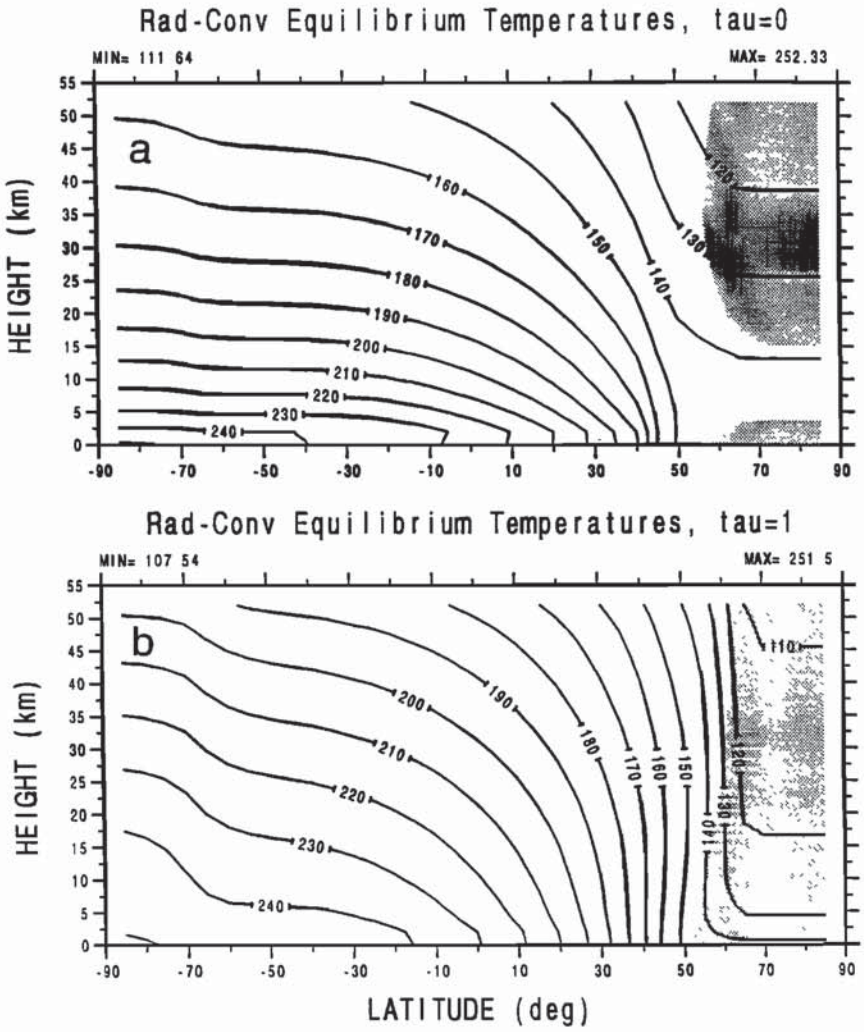


**Figure 1.** Radiative-convective equilibrium temperatures at winter solstice ($L_s$ = 270) for (a) a clear atmosphere and (b) a dusty atmosphere with visible optical depth of one. Shaded regions indicate that temperatures are below the local frost point of $CO_2$.

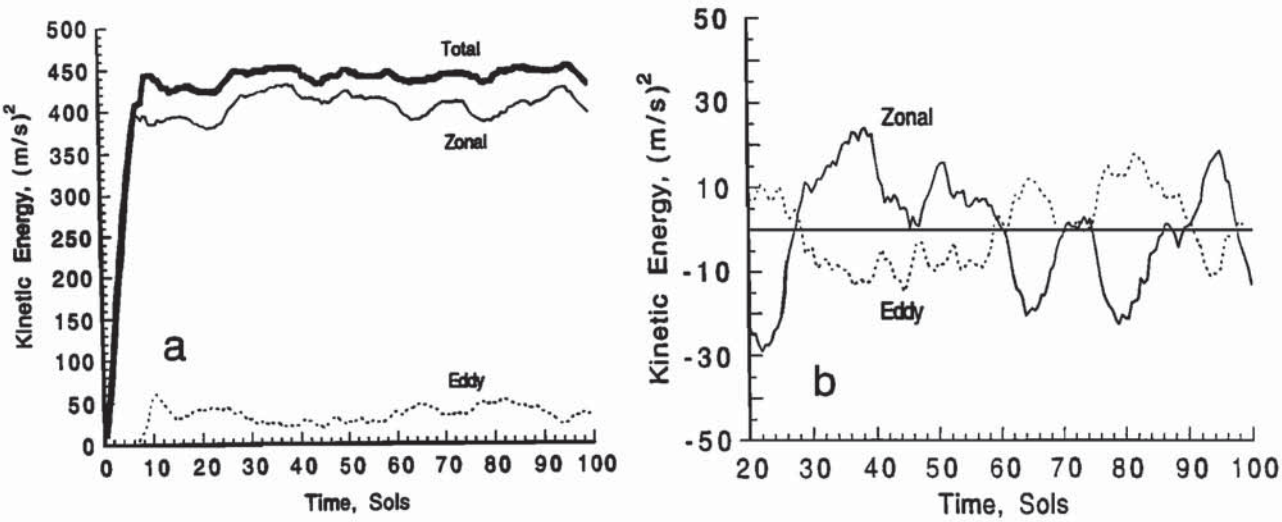


**Figure 2.** (a) Globally averaged total, zonal, and eddy kinetic energies for the clear atmosphere 2-day thermal damping time. (b) Departures of the zonal and eddy kinetic energy from their time mean values for the last 80 days.

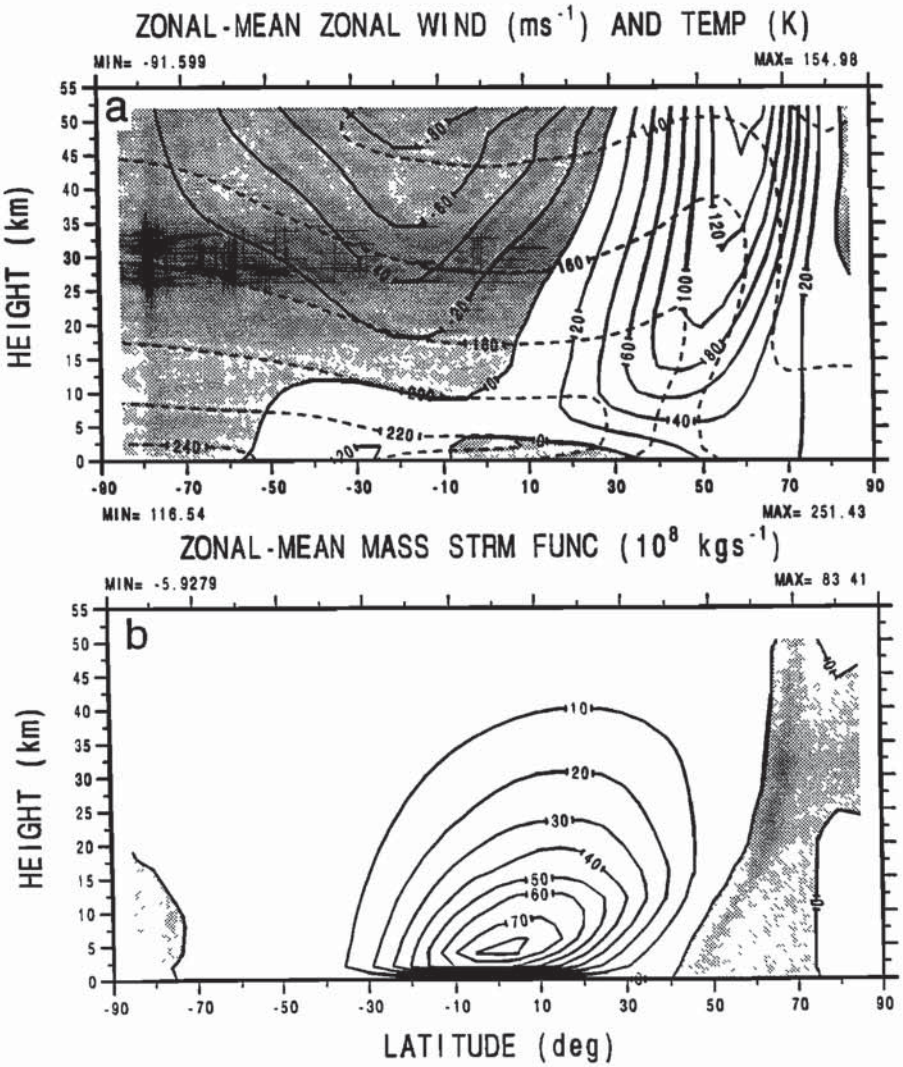


**Figure 3.** (a) Time and zonally averaged temperature and zonal wind fields and (b) mass stream function field for the clear atmosphere 2-day damping time experiment. In Figure 3a, zonal wind contours are solid lines, while temperature contours are dashed lines; shaded regions indicate easterly winds. In Figure 3b, flow is clockwise around positive maxima and counterclockwise around negative minima; shading indicates negative values.

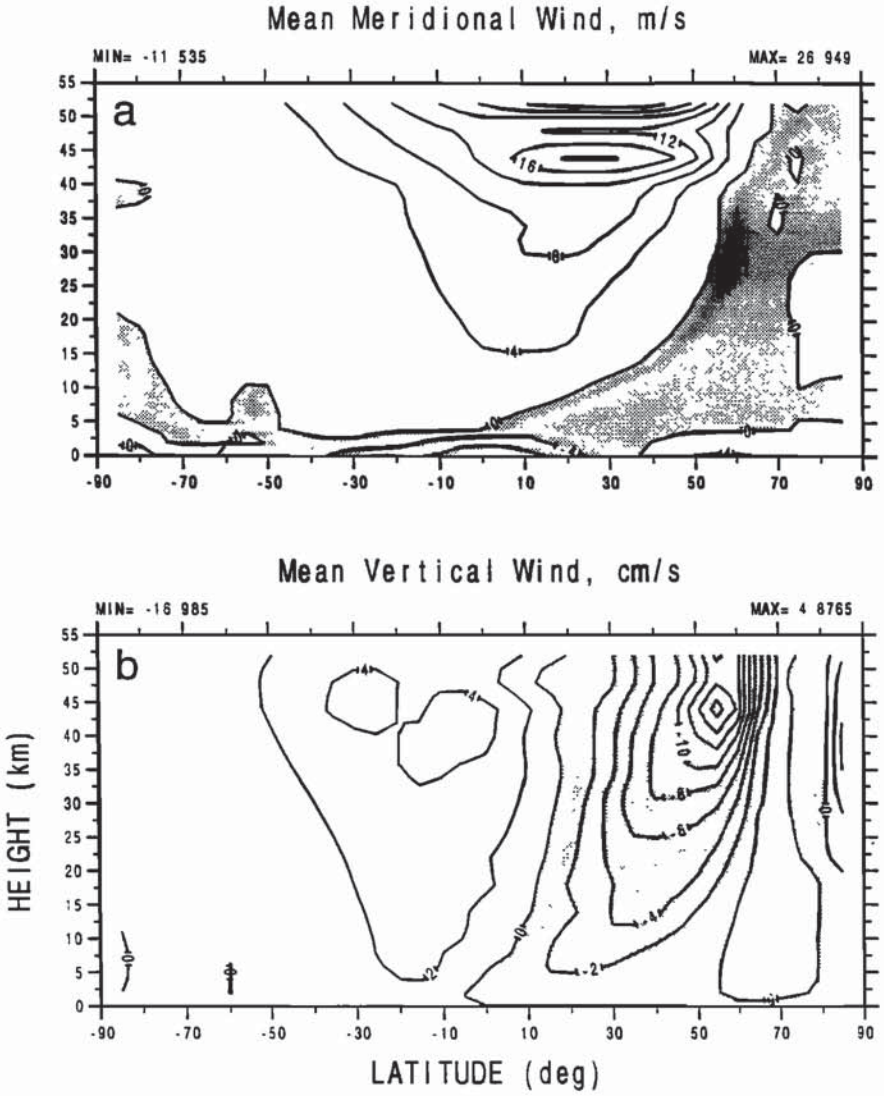


**Figure 4.** (a) Time and zonally averaged meridional and (b) vertical winds for the clear atmosphere 2-day damping experiment. Vertical velocities are positive for ascending motion; meridional velocities are positive for northward motion. In Figures 4a and 4b, shaded regions represent negative values.

$$\frac{\partial(pT)}{\partial t}+\frac{1}{a\sin\theta}\frac{\partial(\sin\theta pvT)}{\partial\theta}+\frac{1}{a\sin\theta}\frac{\partial(puT)}{\partial\varphi}+\frac{\partial(pwT)}{\partial z}$$

$$=-\frac{R}{c_p}pT(\nabla\cdot\vec{v})+\text{heating terms}+\text{damping terms}, \quad (3)$$

$$\frac{\partial(p\Phi)}{\partial z}+\frac{(p\Phi)}{H}=\frac{R}{H}(pT), \quad (4)$$

$$\frac{1}{a\sin\theta}\frac{\partial}{\partial\theta}(\sin\theta pv)+\frac{1}{a\sin\theta}\frac{\partial}{\partial\varphi}(pu)+\frac{\partial}{\partial z}(pw)=0, \quad (5)$$

and represent the zonal and meridional momentum equations, the thermodynamic energy equation, the hydrostatic equation, and the continuity equation, respectively. The independent variables are time $t$, colatitude $\theta$, longitude $\varphi$, and height $z$ defined as

$$z=-H\ln\left(\frac{p}{p_s}\right) \quad (6)$$

where $H$ is a constant (scale height) and $p_s=p_s(\theta,\varphi)$ can be a horizontally varying but time independent surface pressure. In the present work we take $p_s$ to be constant. Subsequent papers will relax this assumption to examine the effects of topography. The dependent variables are $\vec{v}=u\vec{i}+v\vec{j}+w\vec{k}$, the total wind vector which has components $u$ (positive eastward), $v$ (positive southward), and $w=dz/dt$ (positive upward), pressure $p$, temperature $T$, and geopotential $\Phi$. Other variables are $R$, the gas constant; $a$, the planetary radius; and $f=2\Omega\cos\theta$, the Coriolis parameter.

To facilitate solving these equations, the pressure-weighted horizontal velocity components are first expressed in terms of a velocity potential $S$ and stream function $\Psi$

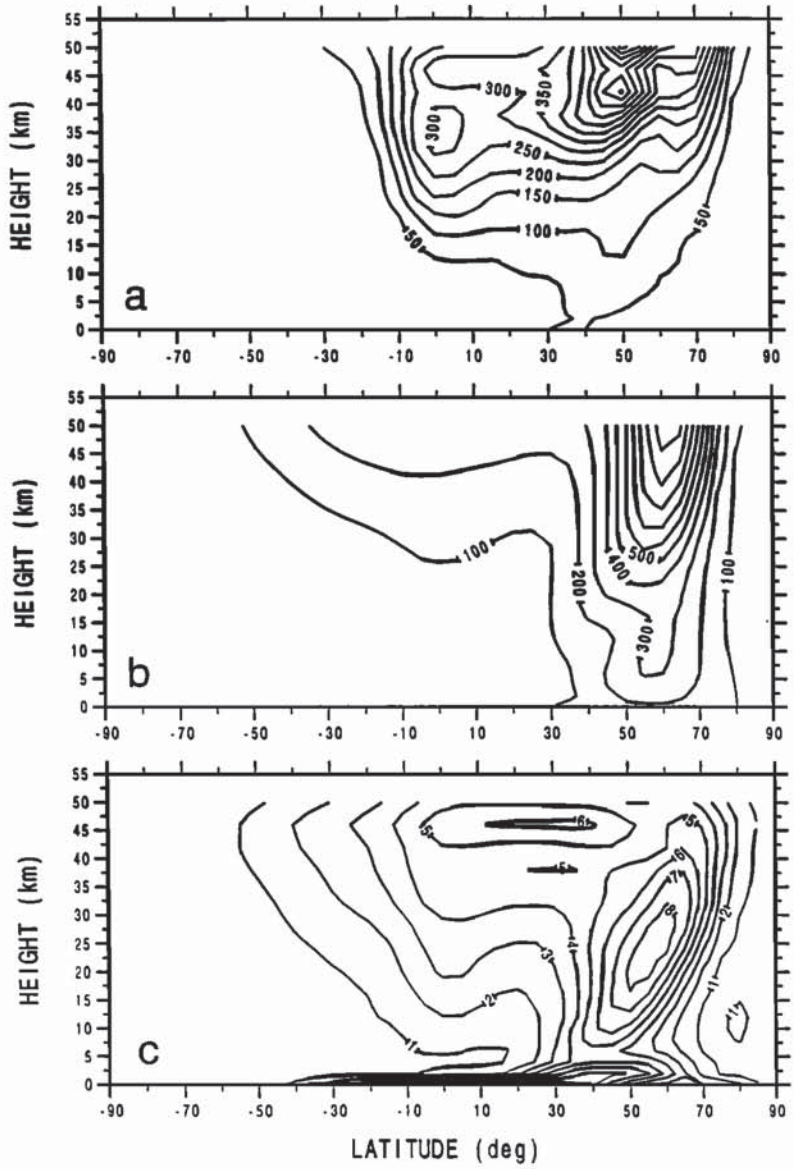


**Figure 5.** Time and zonally averaged eddy statistics for the clear atmosphere 2-day damping time experiment: (a) eddy kinetic energy density, (b) square root of the eddy geopotential height variance, and (c) square root of the eddy temperature variance.

$$pu = -\frac{\partial \Psi}{\partial \theta} + \frac{1}{\sin\theta}\frac{\partial S}{\partial \varphi} \tag{7}$$

$$pv = \frac{1}{\sin\theta}\frac{\partial \Psi}{\partial \varphi} + \frac{\partial S}{\partial \theta} \tag{8}$$

These expressions are then substituted into (1) and (2) which are rewritten in terms of the vertical component of vorticity $\xi = \nabla_H^2 \Psi$, and horizontal divergence $D = \nabla_H^2 S$, where

$$\nabla_H^2 \equiv \frac{1}{a^2 \sin\theta}\frac{\partial}{\partial \theta}\left(\sin\theta \frac{\partial}{\partial \theta}\right) + \frac{1}{a^2 \sin^2\theta}\frac{\partial^2}{\partial \varphi^2} \tag{9}$$

Rewriting the momentum equations in terms of vorticity and divergence is very convenient for semi-implicit spectral models. It also greatly facilitates interpretation of the results because vorticity and divergence are fundamental dynamical quantities.

The variables $S$, $\Psi$, $pT$, $pw$, $p\Phi$, and $p_s$ are then expanded in terms of truncated series of spherical harmonics

$$F(z,\theta,\varphi,t) = \sum_{m=-M}^{M} \sum_{n=|m|}^{N(m)} F_{nm}(z,t) Y_n^m(\theta,\varphi) \tag{10}$$

where $F$ represents any of the above scalar variables and $Y_n^m$ is a spherical harmonic. After multiplying each equation by the complex conjugate of $Y_n^m$ and making use of the normalization properties of the spherical harmonics, we obtain a set of differential equations for the coefficients $F_{nm}$. These equations are solved using the same techniques as described by *Hoskins and Simmons* [1975] and *Gordon and Stern* [1982].

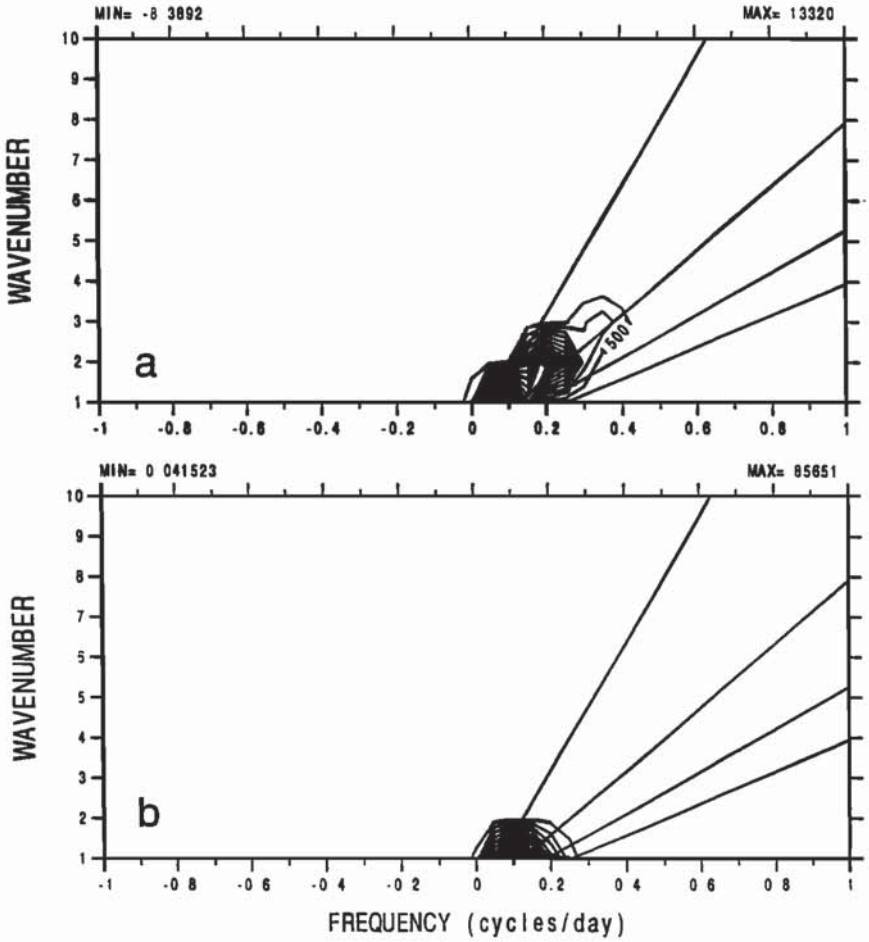


**Figure 6.** Space-time power spectra of the eddy geopotential height for the clear atmosphere 2-day damping time experiment at two different levels: (a) the 3.92 mbar pressure level and (b) the 0.19 mbar pressure level. Both spectra were computed at 50.1°N. The frequency interval is 0.025 cycles $dy^{-1}$. The sloping straight lines correspond to zonal phase speeds of 10, 20, 30, and 40 m $s^{-1}$.

In (10), $M$ and $N(m)$ are the maximum zonal and total wavenumbers, respectively. Equation (10) is written in a generalized form so that three different types of truncation are possible: triangular ($N(m) = M$), rhomboidal ($N(m) =$ const + $m$), and trapezoidal ($N(m) =$ const). In the present work we use trapezoidal truncation with $M = 10$ and $N(m) = 30$. Note that in this truncation the meridional resolution depends on the zonal wavenumber and that it decreases with increasing wavenumber.

The vertical structure of the model consists of 16 layers from the planet's surface to ~55 km. Variables are evaluated in a staggered grid, with $p\Phi$ and $pw$ defined at layer boundaries and $pT$, $S$, and $\Psi$ defined at layer centers. This facilitates the finite difference representation of the vertical derivatives in (1)–(5). The layers are thin near the surface (lowest layer $\approx$ 500 m) to resolve baroclinic waves. The layers widen to a thickness $\approx H/2$ near the top of the model.

## Physical Processes

The heating terms in (3) are due to radiation and latent heat release. Latent heat release occurs whenever atmospheric temperatures fall below the local $CO_2$ frost point temperature $T_f$. Because $CO_2$ is the only atmospheric constituent, enough latent heat is released to maintain temperatures at $T_f$. Radiative heating $J$ is given by

$$J = -\frac{(T - T_e)}{\tau} \tag{11}$$

where $T_e$ is a "relaxation" temperature taken to be the daily and zonally averaged radiative-convective equilibrium temperature and $\tau$ is a thermal damping time taken to be spatially and temporally constant. Nominally, we take $\tau = 2$ days. $T_e$ is calculated off-line using the radiative-convective model of *Haberle and Jakosky* [1991]. The results for a clear and dusty atmosphere at northern winter solstice are given in Figure 1. In calculating these temperatures the surface pressure (6.1 mbar), dust optical depth (0 and 1), soil albedo (0.25), and thermal inertia (272 SI) are assumed to be independent of latitude and longitude. We have also assumed that surface temperatures cannot fall below $T_f$ (= 149 K at 6.1 mbar), while atmospheric temperatures ($T_e$ not $T$) can as is indicated by the shaded regions in Figure 1. This al-

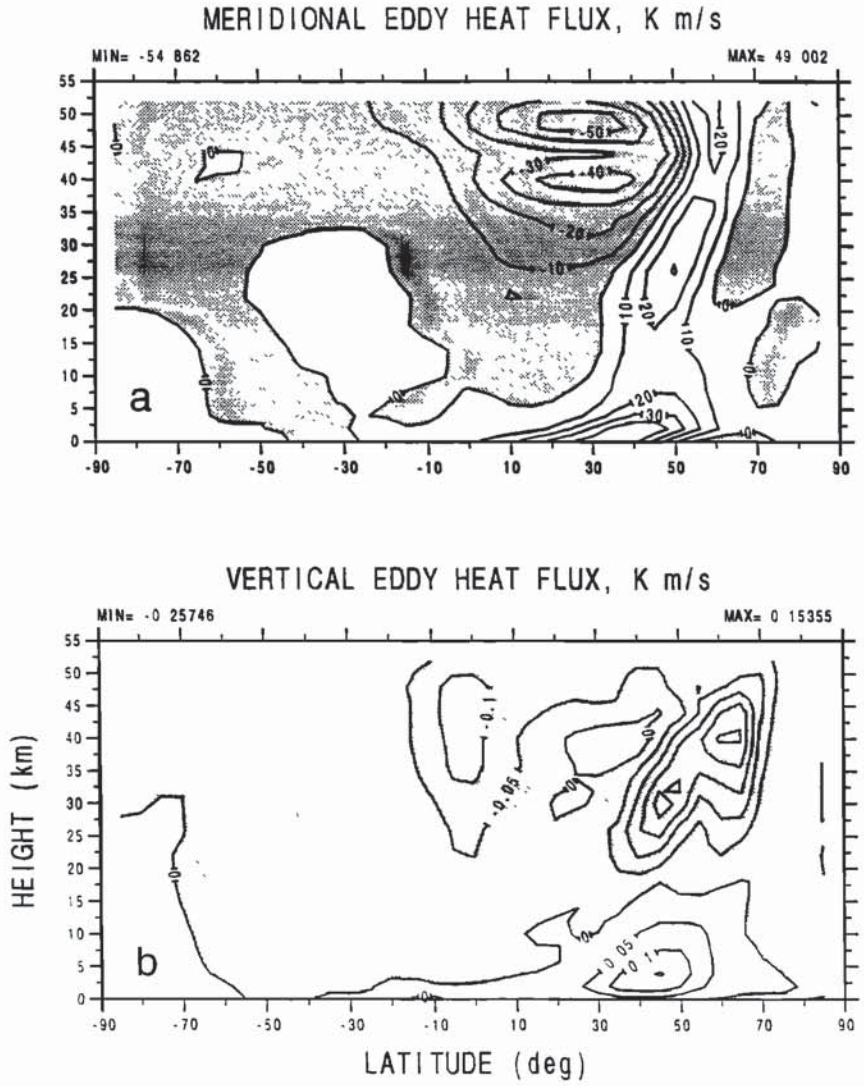


**Figure 7.** (a) Time and zonally averaged meridional and (b) vertical eddy heat fluxes for the clear atmosphere 2-day damping time experiment. Positive values are associated with northward or upward fluxes. In Figures 7a and 7b, shaded regions indicate negative fluxes.

lows us to better represent atmospheric $CO_2$ condensation which would otherwise be zero when $T = T_e = T_f$. To include the effect of a condensation flow, we set the (pressure) vertical velocity at the surface at a given latitude equal to that required to remove $CO_2$ from the atmosphere at the rate computed by the radiative-convective model. (This vertical velocity is set equal to zero at the top of the model as the upper boundary condition.)

With the above daily average formulation for the radiative forcing, the model has no diurnal cycle. How this affects the mean circulation and the eddies important to tracer transport is the subject of the next section where model results are compared with the Ames GCM [*Pollack et al.*, 1990].

The model uses Rayleigh friction in the top three layers and a quadratic drag in the bottom two layers. At all other levels the atmosphere is inviscid. The damping time increases exponentially from 3 days in the top layer to 8.15 days in the third layer down. At the surface the damping time is 10 days in the bottom layer (10 m $s^{-1}$ wind) and 27.2 days in the next layer up.

The model also uses a $\nabla^8$ hyperdiffusion for internal dissipation. For our standard run the diffusion coefficient is taken to be $5.5 \times 10^{38}$ $m^8$ $s^{-1}$ which corresponds to a damping time of about 0.8 days for a total wavenumber of 10. For our dusty and reduced resolution runs we found we needed a diffusion coefficient 10 times larger to prevent nonlinear instability.

## Results

The model is spun up from a resting isothermal (200 K) state and run for 100 days. Output is sampled twice a day and statistics are generated from the last 80 days.

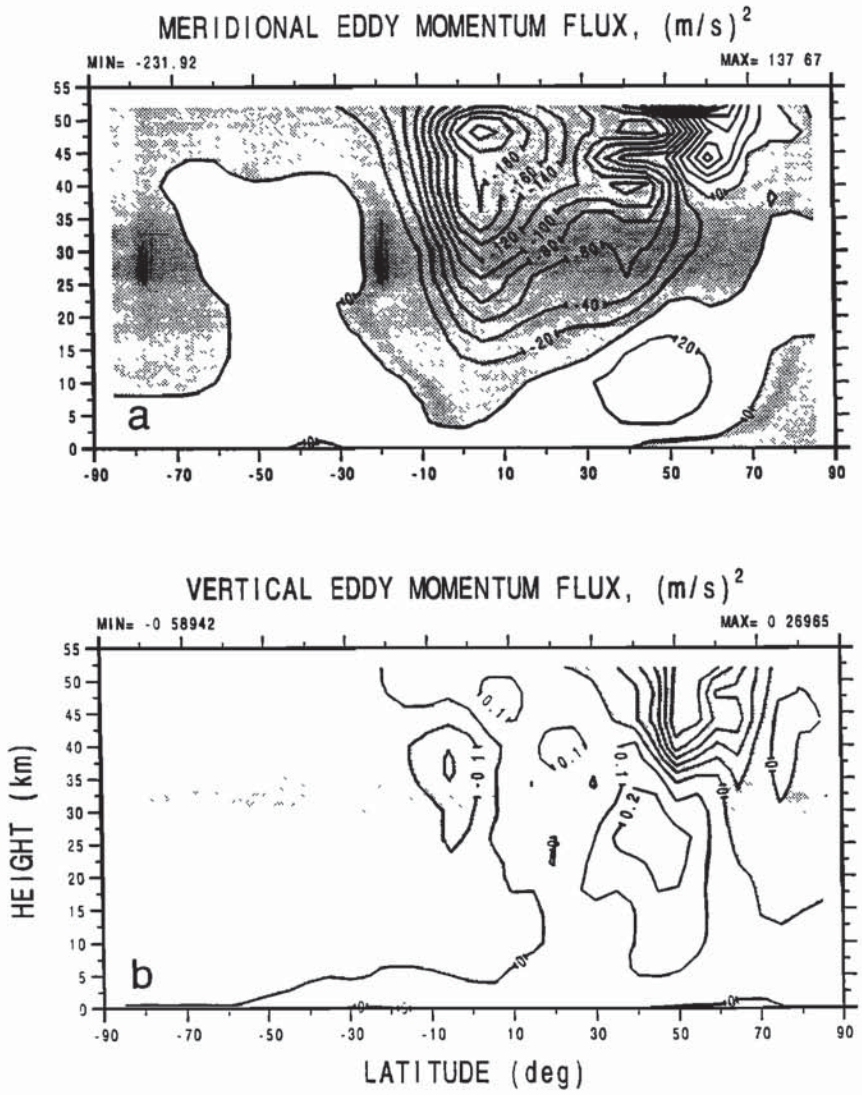


**Figure 8.** Same as Figure 7, but for momentum.

### Clear Atmosphere

We discuss first the results for a clear atmosphere with a 2-day thermal damping time. The circulation ramps up quickly for this experiment and is in quasi-equilibrium by sol 15 (Figure 2). At equilibrium, fluctuations in the zonal and eddy kinetic energy are negatively correlated and of relatively small amplitude ($\sim 20$ m$^2$ s$^{-2}$) and have a dominant period around 20 days. Most of the energy is taken up by the mean flow as the ratio of zonal kinetic-to-eddy kinetic energy is about 12. Not surprisingly, this ratio is higher than found in the Ames GCM [*Haberle et al.*, 1993] which includes other types of eddy activity such as stationary waves and thermal tides.

The mean flow fields are shown in Figures 3 and 4. Temperatures and zonal winds exhibit the same basic structure as found in other models. In the southern hemisphere the static stability is low, and easterlies dominate, except for a low level westerly jet at subtropical latitudes. In the northern hemisphere the static stability is high, westerlies dominate, and the jet axis slopes poleward with latitude. The strength of the jet at 40 km ($\sim 120$ m s$^{-1}$) is about 50% greater than that found in the Ames GCM for clear conditions (not published) but is in good agreement with the simulation using a low (0.3) dust optical depth [*Haberle et al.*, 1993].

In both hemispheres, temperatures increase with latitude, but for different reasons. Radiation controls the thermal structure in the southern hemisphere, while dynamics controls it in the northern hemisphere. The latter is the result of a large cross-equatorial Hadley circulation which has its rising branch in the southern hemisphere and its descending branch in the northern hemisphere. The horizontal and vertical motions associated with this Hadley circulation are relatively weak in the lower atmosphere but sizable in the upper atmosphere where Rayleigh friction is significant (Figure 4).

In Figure 3, note the presence of a strong low level inversion in the zonal mean temperature field between +30° and -30°. While the temperature field we are relaxing to has a similar feature (Figure 1), it is not nearly as strong

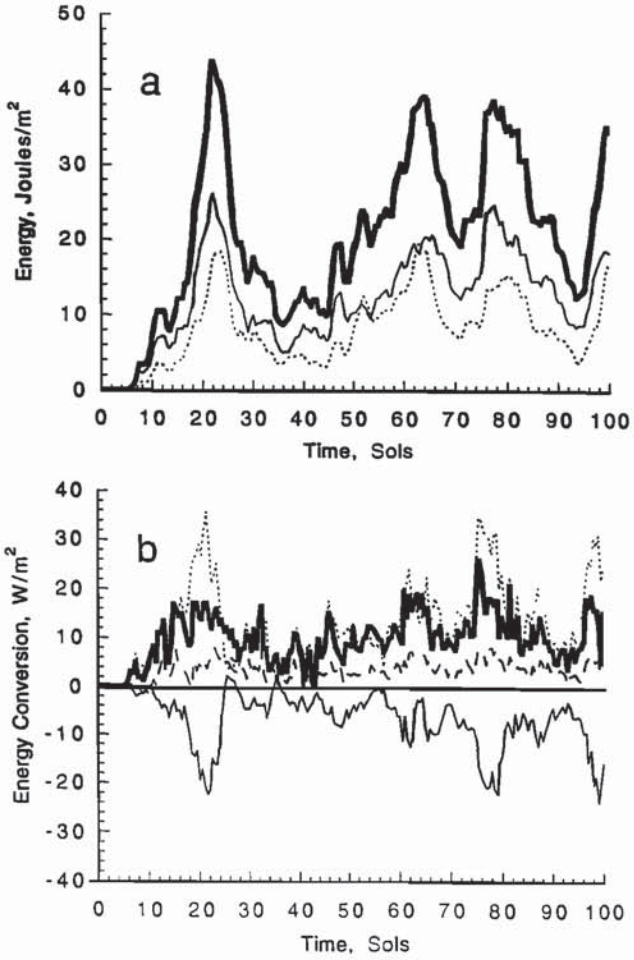


**Figure 9.** Wave 1 (a) energies and (b) energy conversions for the clear atmosphere 2-day damping time experiment. Curves in Figure 9a are kinetic energy (thin solid), potential energy (thin dotted), and total energy (thick solid). Curves in Figure 9b are baroclinic conversion of eddy available to eddy kinetic energy (thin solid); barotropic conversion of zonal kinetic to eddy kinetic energy (thin dotted); wave-wave conversion of eddy kinetic energy from all other waves into eddy kinetic energy of wave 1 (thin dashed). The total conversion is given by the thick solid line.

as that shown in Figure 3. We attribute the strengthening of the directly forced inversion to the advection of cold air by the mean circulation since the timescale for overturning is comparable to the thermal damping time. However, the presence of this inversion appears to be independent of the damping time. Experiments with a 1-day and 4-day damping time (not shown) have low level tropical inversions similar to those shown in Figure 3. As the damping time decreases (increases), temperatures relax quicker (slower) to their equilibrium values, but this is apparently compensated by the increase (decrease) in the intensity of the circulation and therefore cold air advection. Interestingly, similar (though less intense) low level tropical inversions can be found in more sophisticated models [*Haberle et al.*, 1993; *Hourdin et al.*, 1993].

Selected eddy statistics for this experiment are shown in Figure 5. The eddies have deep structures and are most prominent at high northern latitudes. However, significant activity is evident at upper levels in the tropics, particularly in the kinetic energy field, and this may be the response of an inertially unstable tropical atmosphere to midlatitude forcing. *Barnes et al.* [1993] discuss this possibility for the Ames GCM. Given the similarity in mean fields between the two models, it seems plausible that this might also be occurring in the climate model.

The structure and magnitude of the variances shown in Figure 5 are similar (but generally larger) to those produced by the Ames GCM [see *Barnes et al.*, 1993, Figure 9]. The main difference is near the surface where eddy temperature amplitudes in the climate model are largest at lower latitudes. This pattern is absent in the Ames GCM and is probably related to the climate model's strong low-latitude inversion. Though inversions tend to reduce baroclinic activity, the lack of vertical mixing in the climate model must play a role.

Space-time power spectra shown in Figure 6 indicate that the eddies are eastward-propagating disturbances with relatively low zonal wavenumbers (1–3). Very little variance is present at wavenumbers greater than 3. Wavenumber 1

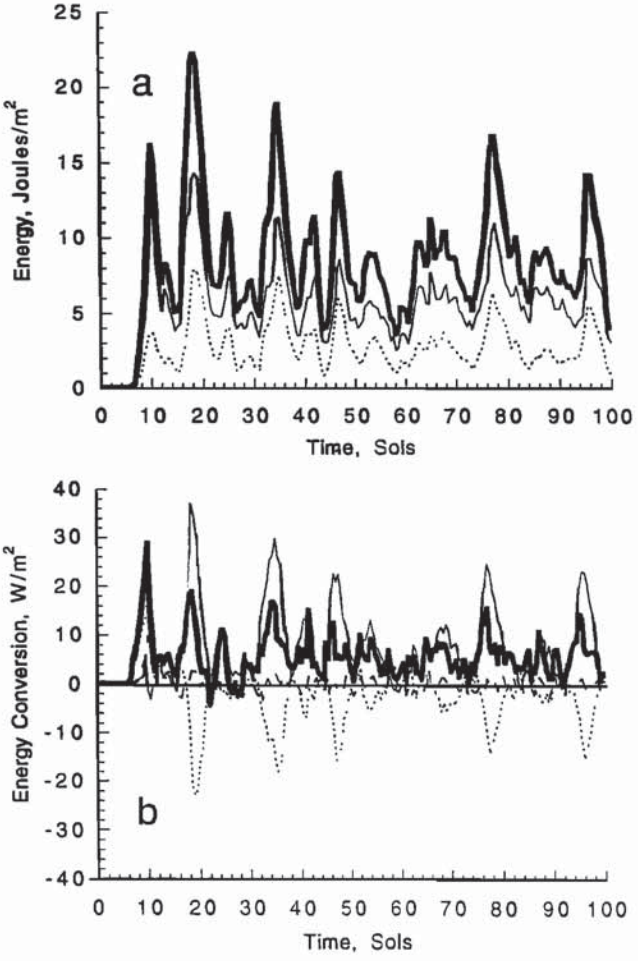


**Figure 10.** Same as Figure 9, but for wave 3.

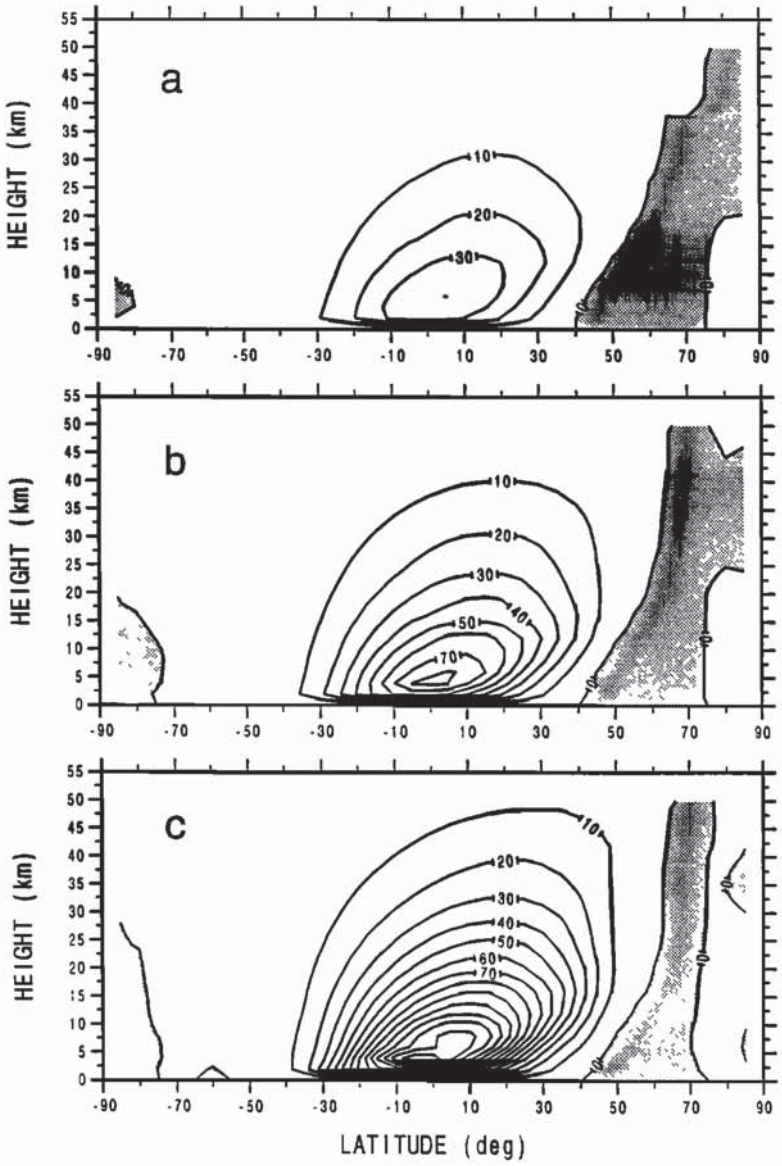


**Figure 11.** Time and zonally averaged mass stream function for the (a) 4-day, (b) 2-day, and (c) 1-day clear atmosphere thermal damping time experiments.

has a period of about 10 days and is prominent at all levels; wavenumbers 2 and 3 have shorter periods (2–5 days) and are prominent only in the lower atmosphere. These wavenumbers and periods are consistent with a constant zonal phase speed of 15–20 m $s^{-1}$, somewhat lower than that found in the Ames GCM at a similar latitude and level but within the range of that inferred from lander data [*Barnes*, 1981]. For this particular latitude (50.1°N), these phase speeds suggest a very low steering level (see Figure 2). We suspect that much of the difference in the transient eddies in the climate model and GCM is related to the topography which appears to be important in the GCM.

The eastward propagating aspect of the eddies suggests they are traveling baroclinic waves and this is at least partly consistent with the eddy heat and momentum fluxes shown in Figures 7 and 8. At northern midlatitudes the waves transport heat poleward throughout the entire depth of the model domain. In the lowest several scale heights of this region they also transport momentum poleward and heat upward. These are the classical signatures of baroclinic waves. However, above this region the eddy heat fluxes are downward, and the momentum fluxes are equatorward. In this region the eddies appear to have a mixed baroclinic/barotropic character. A similar situation was found in the Ames model [*Barnes et al.*, 1993]. However, in the Ames GCM the vertical eddy heat fluxes were upward at all levels in northern midlatitudes, in sharp contrast to the climate model results. Furthermore, the climate model heat fluxes are about twice as large as those in the Ames GCM, suggesting a different phasing between the wind and temperature fields. The verti-

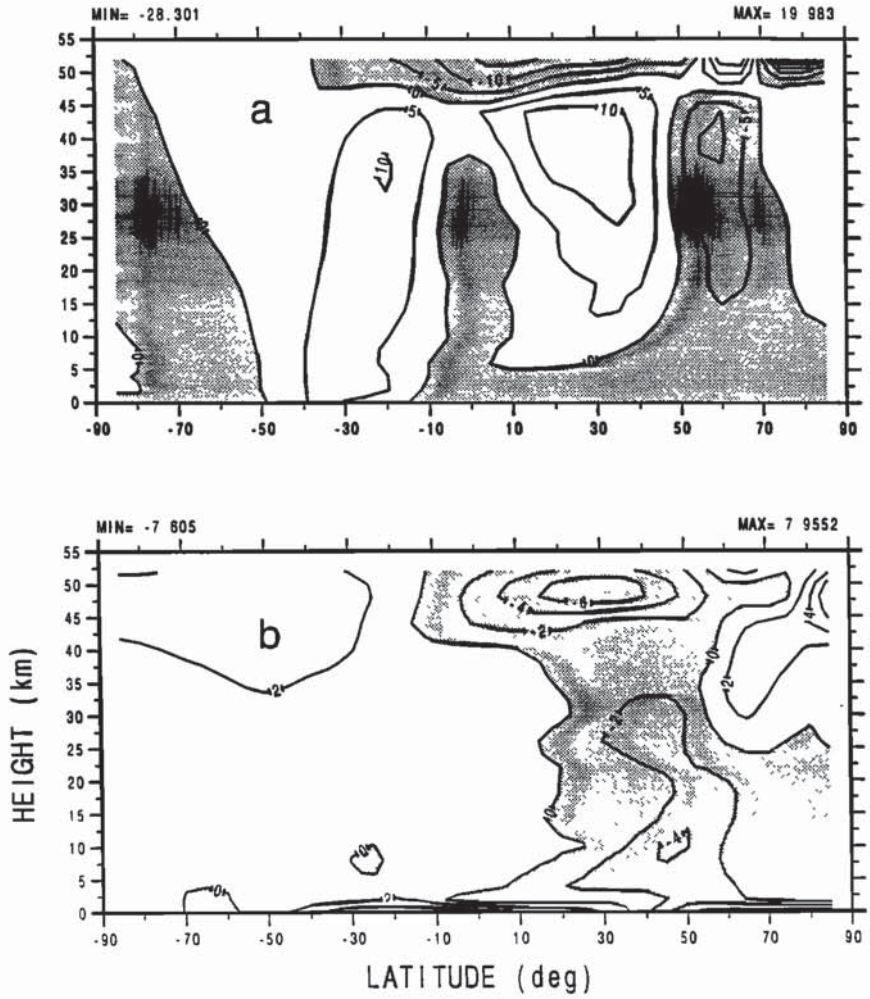


**Figure 12.** Changes in the (a) time and zonally averaged zonal wind and (b) temperature fields when the thermal damping time is lowered from 2 days to 1 day.

cally integrated eddy heat and momentum fluxes (not shown) have peak values that are similar to those in the Ames GCM. This indicates that the large poleward heat fluxes in the lower levels of the climate model are nearly compensated for by the large equatorward fluxes at upper levels. A similar situation must also exist for momentum.

The mixed baroclinic/barotropic nature of the eddies can be further illustrated from their energetics. Figures 9 and 10 show the global mean energy and energy conversions for waves 1 and 3, respectively. Both waves exhibit significant, though irregular, life cycle behavior. For wave 1, growth is accomplished by the conversion of zonal mean kinetic energy to eddy kinetic energy, and decay by the conversions of eddy kinetic energy to eddy available potential energy. Thus wave 1 grows barotropically and decays baroclinically. However, the opposite is true for wave 3. Since wave 3 is vertically trapped and wave 1 is not (Figure 6), it seems likely that the baroclinic signatures in the heat and momentum fluxes of the lower atmosphere are due to the shorter waves, while the barotropic signatures in upper atmosphere are due to the longer waves.

### Thermal Damping Time

We now examine how the circulation is affected by a change in the thermal damping time. This is the single most important free parameter in our simplified model, and its effects need to be thoroughly understood. Thus we have carried out experiments for thermal damping times of 1 day and 4 days to illustrate the effects of a more rapid, and more sluggish, relaxation to the input temperature field.

The main effect of this parameter on the mean fields is to change the intensity of the mean meridional circulation (Figure 11). The structure is hardly affected since the relaxation temperature field is unchanged. For a 1-day damping time the peak tropical mass flux is $150 \times 10^8$ kg s$^{-1}$, while at 4 days it is $40 \times 10^8$ kg s$^{-1}$. For the range of damping times we have considered, the peak mass flux scales linearly with the inverse damping time. This kind of scaling is expected for nearly inviscid flows in which radiative heating is balanced by adiabatic cooling [e.g., *Held and Hou,* 1980]. Such flows also conserve angular momentum so that the mean zonal wind and temperature fields are controlled by

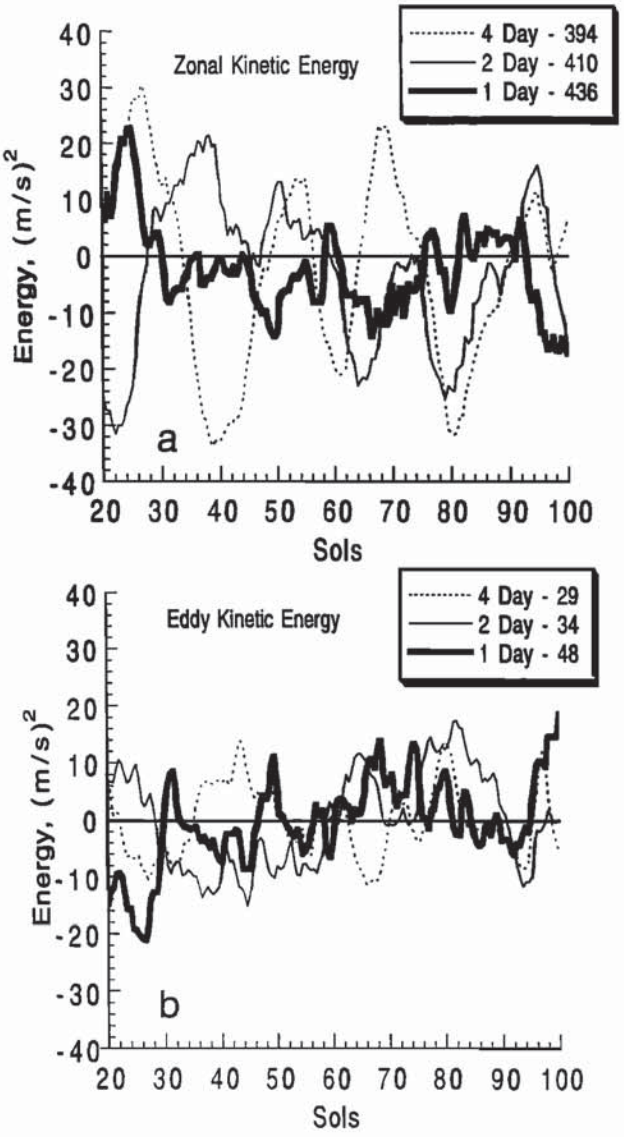


**Figure 13.** Fluctuations in the (a) globally averaged zonal and (b) eddy kinetic energy for each of the clear atmosphere thermal damping time experiments. The mean for each (indicated by the number following the dash in the legend) has been removed.

this constraint rather than the heating distribution. This too is consistent with our results wherein the peak zonal wind speed of $\approx$ 120 m $s^{-1}$ near 60° latitude (Figure 3) is equal to the difference between the surface rotational speeds at the equator and 60°. As a result, our model shows only small changes in the zonal wind and temperature fields with damping time (Figure 12).

For damping times between 2 and 4 days, we also find very little change in basic eddy statistics, but for shorter damping times the eddies become increasingly vigorous. For the 1-day damping time experiment the time-averaged eddy kinetic energy increases by 40% from its corresponding value in the 2-day experiment. This is illustrated in Figure 13 which also shows fluctuations in zonal and eddy kinetic

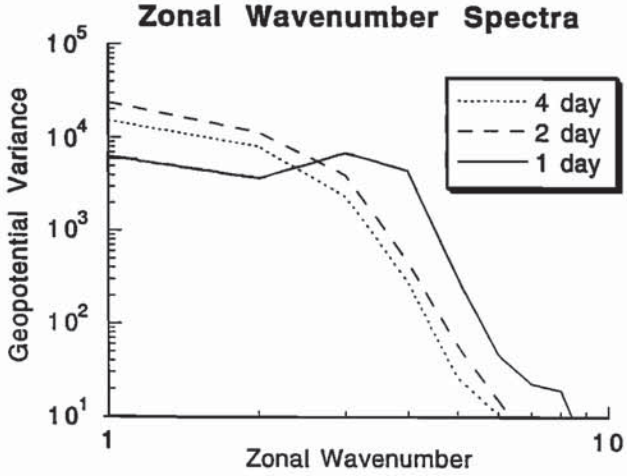


**Figure 14.** Zonal wavenumber power spectra of the geopotential height variance at 50.1°N and a pressure level of 3.92 mbar.

energy about their mean values. The mean for both components increases with decreasing damping time, though the increase is proportionately larger for the eddies. Interestingly, the amplitude of eddy fluctuations is less affected by the damping time than that for zonal fluctuations. In the latter case, the fluctuations are large and quasi-regular in the 4-day experiment but small and somewhat irregular in the 1-day experiment. Thus shorter thermal damping times appear to have a greater effect on the mean circulation than on the eddies.

There is, however, a change in the dominant zonal wavenumber of the eddies as the damping time decreases. As shown in Figure 14, at low levels in northern midlatitudes, most of the power in the 2-day and 4-day experiments is contained in eddies with dominant zonal wavenumbers between 1 and 2, but for the 1-day case, peak power resides in disturbances with dominant zonal wavenumbers between 3 and 4.

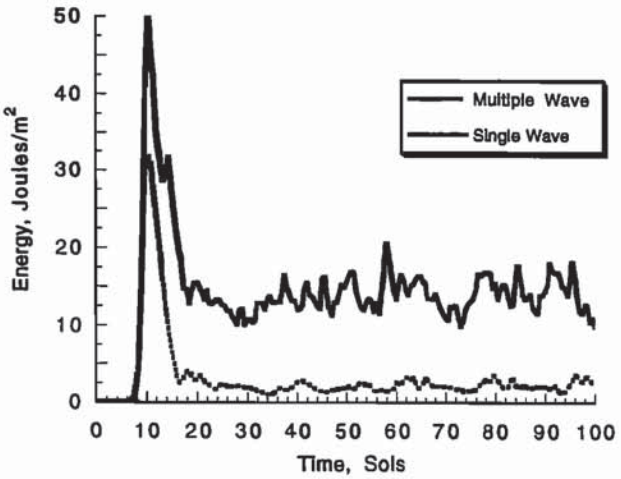


**Figure 15.** Time evolution of eddy kinetic energy of wavenumber 4 for the single wave experiment (solid) and full wave experiment (dashed). Both experiments were run using a 2-day thermal damping time.

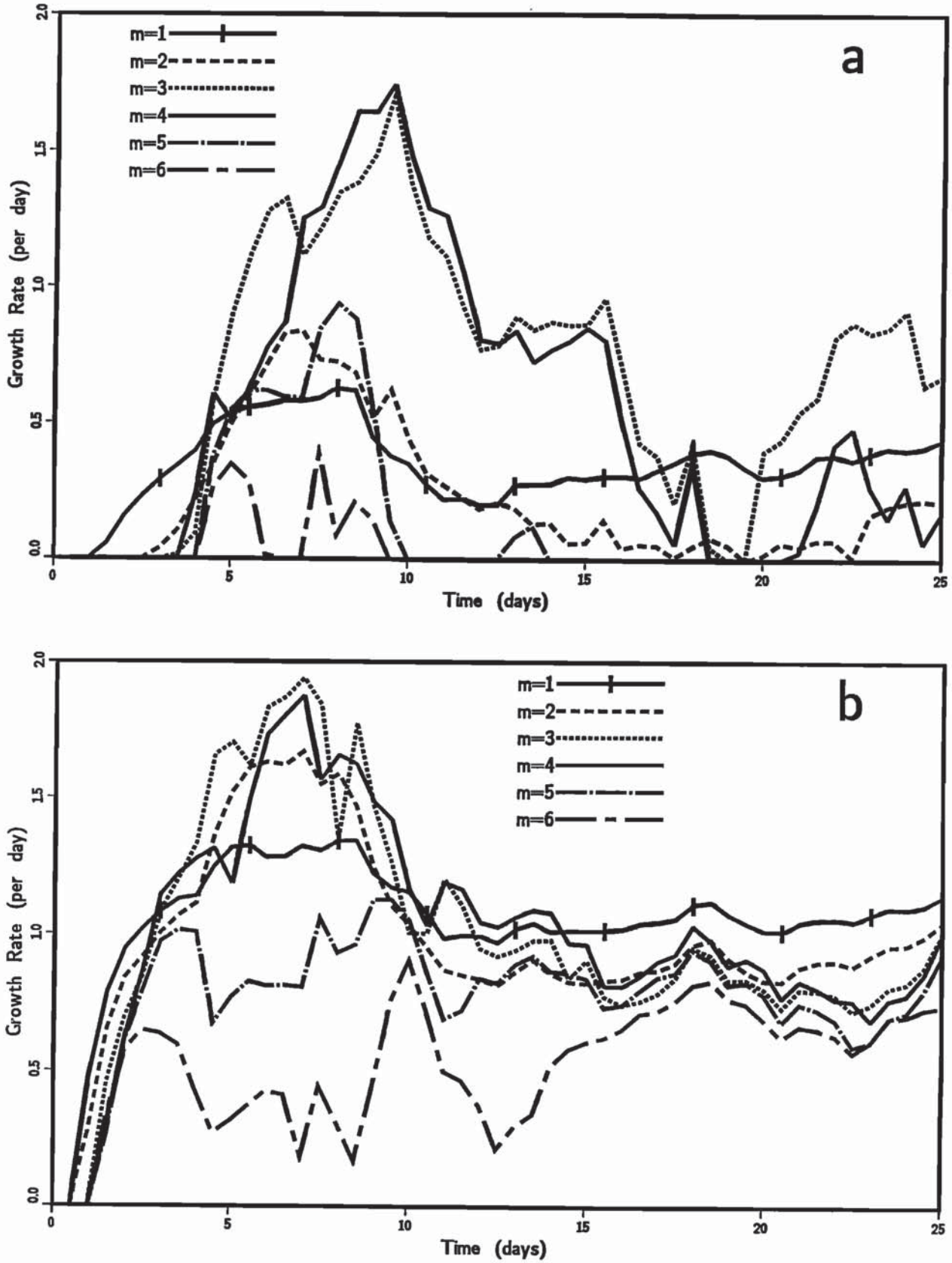


**Figure 16.** (a) Maximum growth rates of waves 1 through 6 for the first 25 sols of the clear atmosphere 2-day damping time experiment. (b) Same as in Figure 16a but with the surface zonal wind component removed from the zonal wind field.

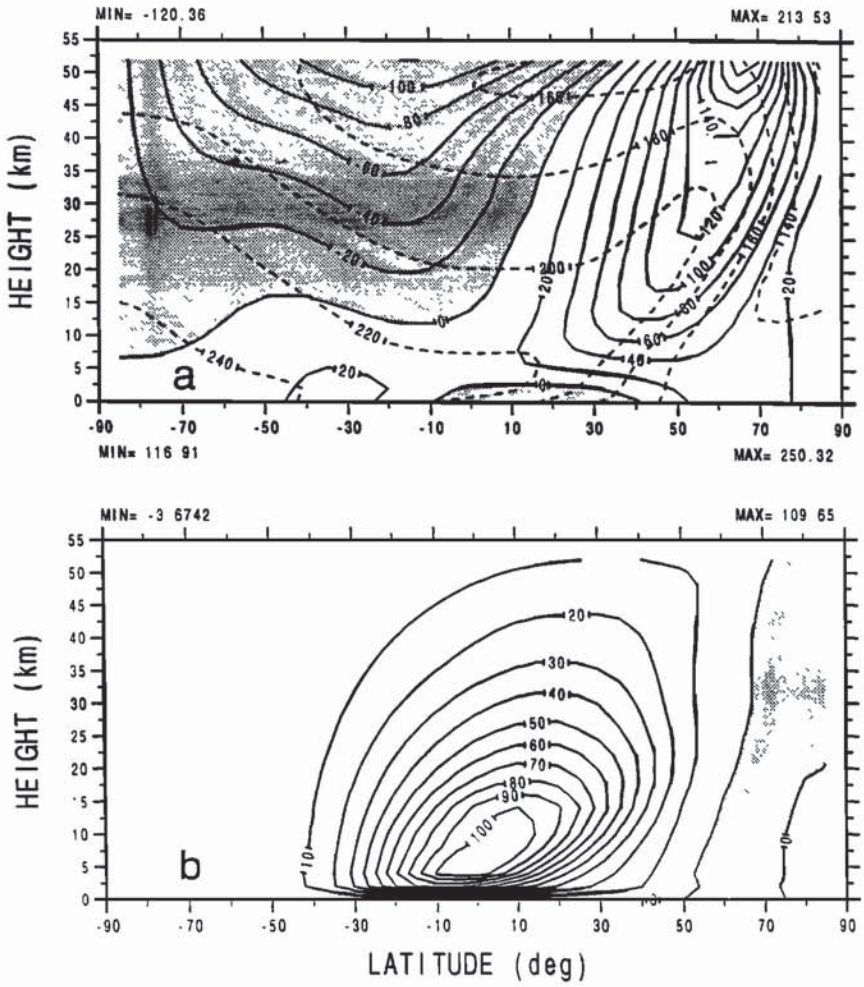


**Figure 17.** Same as Figure 3 but for the dusty simulation.

The shift to higher wavenumbers with increased damping is at least partly due to the inability of the long waves to stabilize the flow. In the presence of strong damping, the mean flow is restored to its basic state faster than the eddies can modify it. This is illustrated in Figure 15 which shows the evolution of wave 4 eddy kinetic energy for two experiments: one in which wave 4 alone is present, and one in which all waves are present (up to our truncation limit of wavenumber 10). In both experiments, wave 4 grows rapidly between day 8 and 12. Afterward, it dies off just as rapidly, but in the single wave case it equilibrates at a level about 5 times as energetic as in the multiple wave case. This implies that the full spectrum of waves stabilizes the basic state to short wave disturbances. Since the longer waves ($m < 4$) are much more energetic than the shorter waves ($m > 4$), we infer that the long waves are stabilizing the flow.

A possible mechanism by which the long waves stabilize the flow to the higher wavenumbers is the barotropic governor [*James and Gray,* 1986]. The linear stability calculations shown in Figure 16 lend some support to this view. Maximum growth rates for waves 3 and 4 exceed 1.5 $dy^{-1}$ on day 10 but then fall to generally smaller values and undergo life cycle like behavior for the rest of the simulation (Figure 16a). However, with the barotropic component of the flow removed, the same calculations show maximum growth rates for waves 3 and 4 that are consistently near 1 $dy^{-1}$ after day 10 (Figure 16b). Of course, it also appears that all waves are stabilized when the barotropic component of the flow is included in the calculations.

### Dusty Atmosphere

We now examine how the climate model responds to a heating field more representative of dusty conditions (optical depth one). This was done by running the model for 100 sols using the relaxation temperature field shown in Figure 1b along with a 1-day thermal damping time.

The change in the mean fields is similar to that seen in the Ames Mars GCM [*Haberle et al.,* 1993]. Zonal winds are strengthened and the mean meridional circulation intensifies and expands (Figure 17). However, zonal wind changes are less pronounced in the climate model. In the GCM the westerly zonal jet at 40 km increases from 120 m $s^{-1}$ for a relatively clear atmosphere (optical depth 0.3) to about 160 m $s^{-1}$ for a moderately dusty atmosphere (optical depth 1).

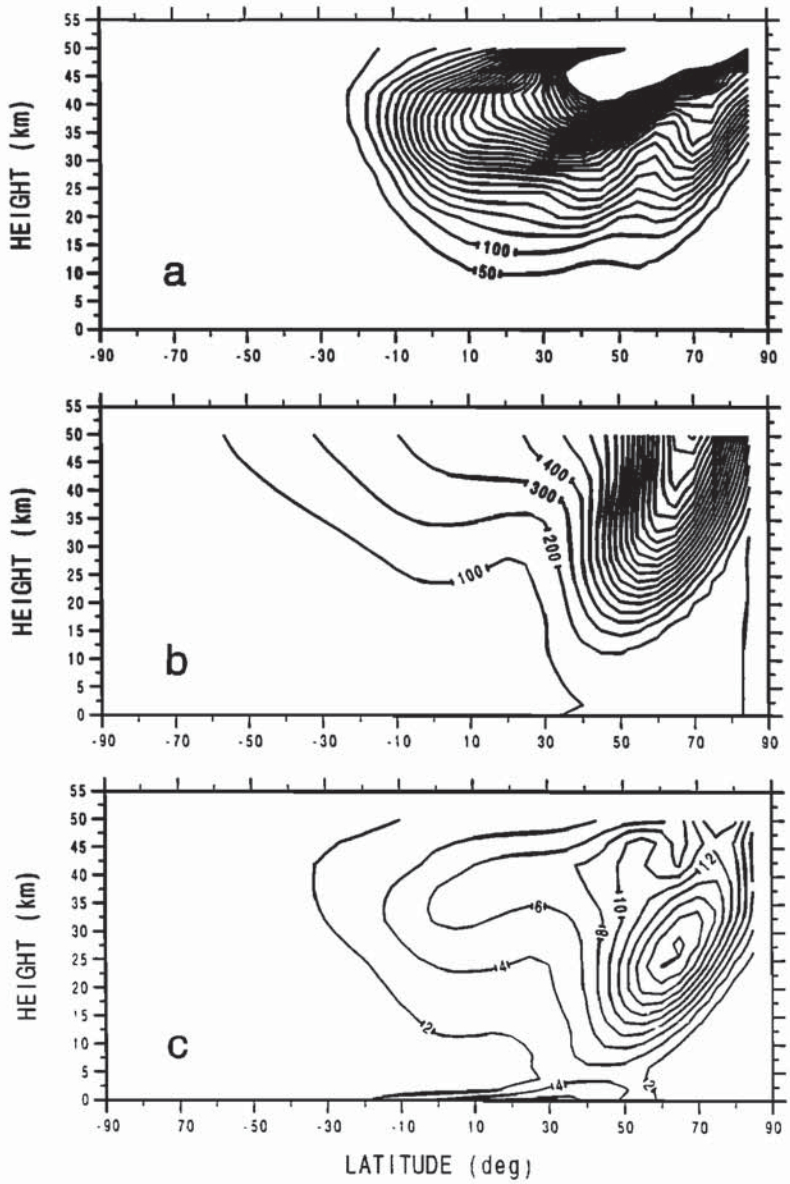


**Figure 18.** Same as Figure 5 but for the dusty simulation.

At that same level in the climate model the increase is only about 10–20 m $s^{-1}$. Note, however, that the climate model has a greater vertical extent and so its sponge layer is higher than in the GCM. Indeed, the greatest change in the zonal wind field in the climate model occurs at the highest model levels.

On the other hand, the approximate 30% increase in the strength of the mean meridional circulation in the climate model is quite close to the increase simulated by the Ames GCM. It is also worth noting that the mean meridional circulation shown in Figure 17b is not as intense as it is for clear conditions with a 1-day damping time (see Figure 11c). This illustrates that the thermal relaxation field also plays a role (besides the damping time) in determining the strength of the overturning flow. The dusty relaxation field of Figure 1b has a much higher static stability than the corresponding clear field of Figure 1a, and this tends to suppress vertical motions.

At low levels, eddy amplitudes and variances are somewhat reduced in our dusty simulation, but higher up they are considerably strengthened (compare Figure 18 with Figure 5). These changes are similar to those seen in the Ames GCM though in the GCM eddy amplitudes and variances at low levels are relatively unchanged, and the eddies have less latitudinal tilt with height than shown in Figure 18. Space-time spectral analysis of eddy geopotential at the same altitude and latitude as shown in Figure 6 further indicate that the low level eddies have a more prominent wave 3 component and that its phase speed has slowed with respect to the clear simulation. An increase in the dominant wavenumber, a decrease in eddy phase speeds, and a reduction in eddy amplitudes was detected in the Viking Lander observations

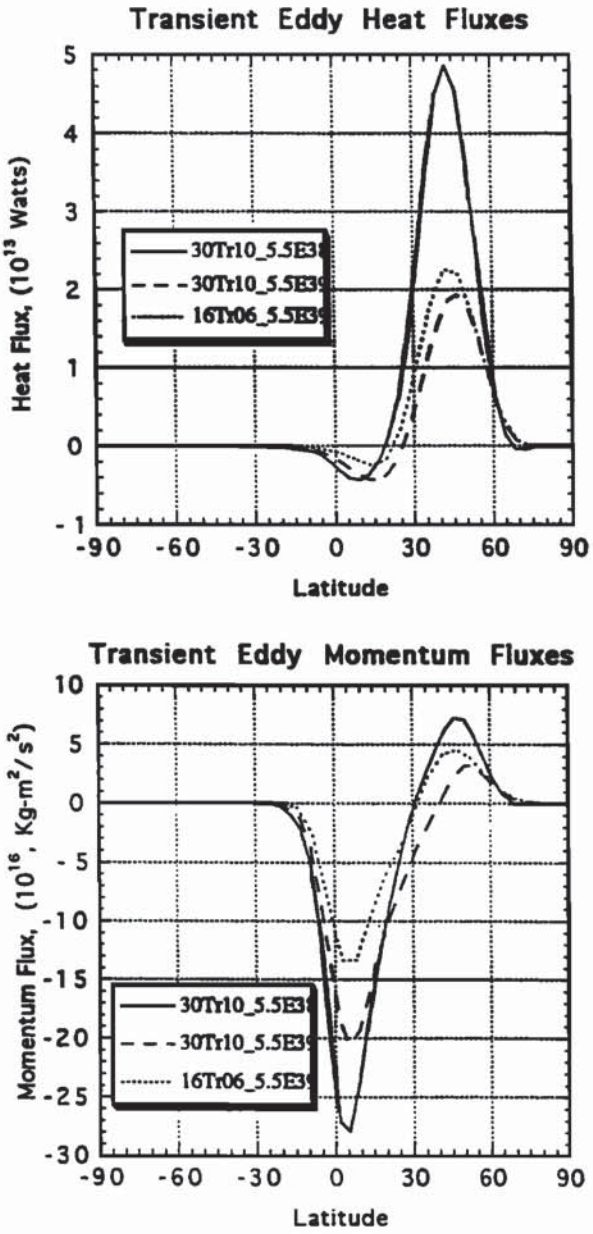


**Figure 19.** Vertically integrated eddy heat and momentum fluxes from the clear simulation for different resolutions and internal diffusions.

during the second global dust storm of 1977 [*Barnes*, 1980, 1981]. However, the observed reduction in eddy variances (pressure in particular) is much greater than simulated by the climate model. Finally, the climate model eddy heat and momentum fluxes are stronger in the dusty simulation (not shown) and retain the mixed baroclinic/barotropic character as in the clear simulation. This too is evident in the GCM.

### Degraded Resolution

Ultimately, our goal is to conduct very long-term simulations of the climate system. This will require that we run at the lowest resolution possible. We have therefore examined the model's performance at a truncation of 16Tr6 with 14 instead of 16 vertical layers (the top two layers were removed). This truncation gives a latitude-longitude resolution of ~7.5°–18°.

In general, the 16Tr6 run shows time and zonal mean flows that are only slightly different from the 30Tr10 run. The zonal jets, for example, are reduced about 5%, and the mean circulation is weakened about 10%. The main change between the 30Tr10 and 16Tr6 runs is the reduction in eddy heat and momentum transports. As shown in Figure 19, the vertically integrated transports can be reduced by as much as a factor of 2. However, this reduction is not due to the degraded resolution. As can also be seen in Figure 19, these fluxes are reduced even at 30Tr10 truncation when the internal diffusion is the same as that required for the 16Tr6 run. In other words, the eddies are more sensitive to diffusion than resolution.

We have no way to assess the significance of this result. On one hand, the eddy fluxes in the low-diffusion 30Tr10 run are quite similar to those found in the Ames GCM, and this would imply that the high-resolution low-diffusion model might be more appropriate for conducting transport studies. On the other hand, we do not know what the real fluxes are, and a factor of 2 difference might not be that significant given the many simplifications we have made in developing this model. We simply note that this is an issue we plan to investigate further.

## Conclusion

We have developed a simplified 3-D global circulation model that is capable of simulating some of the main components of the Martian general circulation as we currently understand it. The model is spectral, uses semi-implicit time differencing, and is forced with Newtonian cooling, Rayleigh friction, and quadratic drag near the surface. In assessing the model's performance, we have compared its results at northern winter solstice with the NASA Ames Mars GCM and with data where available. By tuning the model's most important free parameter, namely, the thermal damping time, we were able to generate a global circulation field that bears remarkable similarity to the Ames GCM. The structure and strength of the mean fields and transient eddies produced by this "climate" model agree well with the Ames model using a thermal damping time of 2 days for relatively clear conditions and 1 day for moderately dusty conditions. Though the eddy fields appear to be sensitive to the internal diffusion (which must be increased when resolution is decreased), we feel we have a model suitable for conducting studies of transport in the Martian atmosphere. By varying the temperature relaxation field and thermal damping time as functions of time, we are able to generate annual and longer-period meteorological simulations. In addition, the model's simple formulation allows the parameterization of important interactions between the surface and atmosphere. *Houben et al.* [this issue] report the results of the model's application to the current Martian water cycle.

**Acknowledgment.** This work was supported by NASA's Planetary Atmospheres Program under RTOP 154–95–80–05.

## References

Barnes, J.R., Time-spectral analysis of midlatitude disturbances in the Martian atmosphere, *J. Atmos. Sci., 37,* 2002–2015, 1980.

Barnes, J.R., Midlatitude disturbances in the Martian atmosphere: A second Mars year, *J. Atmos. Sci., 38,* 225–234, 1981.

Barnes, J.R., and R.E. Young, Nonlinear baroclinic instability on the sphere: Multiple life cycles with surface drag and thermal damping, *J. Atmos. Sci., 49,* 861–878, 1992.

Barnes, J.R., J.B. Pollack, R.M. Haberle, R.W. Zurek, C.B. Leovy, H. Lee, and J. Schaeffer. Mars atmospheric dynamics as simulated by the NASA/Ames general circulation model, 2, Transient baroclinic eddies *J. Geophys. Res., 98,* 3125–3148, 1993.

Davies, D.W., The Mars water cycle, *Icarus, 45,* 398–414, 1981.

Gordon, C.T., and W.F. Stern, A description of the GFDL Global Spectral Model, *Mon. Weather Rev., 110,* 625–650, 1982.

Haberle, R.M., and B.M. Jakosky, Sublimation and transport of water from the north residual polar cap on Mars, *J. Geophys. Res., 95,* 1423–1438, 1990.

Haberle, R.M., and B.M. Jakosky, Atmospheric effects on the remote determination of thermal inertia of Mars, *Icarus, 90,* 187–204, 1991.

Haberle, R.M., J.B. Pollack, J.R. Barnes, R.W. Zurek, C.B. Leovy, J.R. Murphy, H. Lee, and J. Schaeffer, Mars atmospheric dynamics as simulated by the NASA Ames general circulation model, 1, The zonal-mean circulation, *J. Geophys. Res., 98,* 3093–3123, 1993.

Haltiner, G.J., and R.T. Williams, *Numerical Prediction and Dynamical Meteorology,* 477 pp., John Wiley, New York, 1980.

Held, I.M., and A.Y. Hou, Nonlinear axially symmetric circulations in a nearly inviscid atmosphere, *J. Atmos. Sci., 37,* 515–533, 1980.

Held, I.M., and M.J. Suarez, A two-level primitive equation atmospheric model designed for climate sensitivity studies, *J. Atmos. Sci., 35,* 572–576, 1978.

Hoskins, B.J., and A.J. Simmons, A multi-layer spectral model and the semi-implicit method, *Q. J. R. Meteorol. Soc., 101,* 637–655, 1975.

Houben, H., R.M. Haberle, R.E. Young, and A.P. Zent, Modeling the Martian seasonal water cycle, *J. Geophys. Res.*, this issue.

Hourdin, F., P.L. Van, F. Forget, and O. Talagrand, Meteorological variability and the annual surface pressure cycle on Mars, *J. Atmos. Sci., 50,* 3625–3640, 1993.

Jakosky, B.M., The role of seasonal reservoirs in the Mars water cycle, II, Coupled models of the regolith, the polar caps, and atmospheric transport, *Icarus, 55,* 19–39, 1983.

Jakosky, B.M., The seasonal cycle of water on Mars, *Space Sci. Rev., 41,* 131–200, 1985.

Jakosky, B.M. and R.M. Haberle, The seasonal behavior of water on Mars, in *Mars,* edited by H.H. Kieffer, B.M. Jakosky, C.W. Snyder, and M.S. Matthews, pp. 969–1016, Univ. of Ariz. Press, Tucson, 1992.

James, I.N., and L.J. Gray, Concerning the effect of surface drag on the circulation of a baroclinic planetary atmosphere, *Q. J. R. Meteorol. Soc., 112,* 1231–1250, 1986.

Pollack, J.B., R.M. Haberle, J. Schaeffer, and H. Lee, Simulations of the general circulation of the Martian atmosphere, 1, Polar processes, *J. Geophys. Res., 95,* 1447–1474, 1990.

Young, R.E., and G.L. Villere, Nonlinear forcing of planetary scale waves by amplifying unstable baroclinic eddies generated in the troposphere, *J. Atmos. Sci., 42,* 1991–2106, 1985.

Young, R.E., H. Houben, and O.B. Toon, Radiatively forced dispersion of the Mt. Pinatubo volcanic cloud and induced temperature perturbations in the stratosphere during the first few months following the eruption, *Geophys. Res. Lett., 21,* 369–372, 1994.

J. R. Barnes, Deptartment of Atmospheric Sciences, Oregon State University, Strand Agriculture Hall Rm 326, Corvallis, OR 97331–2209. (e-mail: barnes@ats.orst.edu)

R. M. Haberle and R. E. Young, MS 245–3, NASA Ames Research Center, Moffett Field, CA 94035–1000. (e-mail: haberle@humbabe.arc.nasa.gov; ryoung@humbabe.arc.nasa.gov)

H. Houben, Space Physics Research Institute, 572 Hyannis Drive, Sunnyvale, CA 94087–1315. (e-mail: houben@humbabe.arc.nasa.gov)

(Received June 3, 1996; revised January 31, 1997; accepted February 10, 1997.)